Design and fabrication of 3D-extruded scaffolds for osteochondral tissue engineering: optimization of geometry, curvature, and electroconductivity

Pedro Marcelino
Instituto Superior Técnico, Lisbon, Portugal
December 2021

Abstract
Osteochondral (OC) tissue is a highly complex tissue comprising articular cartilage (AC) and the underlying subchondral bone. Damage to this tissue is associated with the risk of developing osteoarthritic degenerative problems due to the AC limited self-repair capacity. Current therapies still fail to mimic native tissue properties and thus tissue engineering (TE) has emerged as a promising therapeutic alternative. TE strategies are based on cells and engineered biomaterials, in which scaffolds are one essential component. For the manufacture of scaffolds, in recent years, additive manufacturing (AM) techniques have been presenting researchers with added options for a better control over scaffold geometry and for the development of patient tailored designs. Fused deposition modeling (FDM), a form of AM, was used to manufacture the scaffolds. To allow future electrical stimulation (ES) studies in the development of OC tissue, methods for coating poly(ϵ-caprolactone) (PCL) scaffolds with poly (3,4-ethylenedioxythiophene) doped with poly (styrene sulfonic acid) (PEDOT:PSS) were developed. Good coating stability and conductivities in the range 3.0-26 S/cm were obtained in protocols using (3-glycidyloxypropyl) trimethoxysilane (GOPS) and divinyl sulfone (DVS) as dopants, without significant difference between both. Considering the design for curved scaffolds, a mathematical approach was used to determine a radius of 17.064 mm as the smallest that could be manufactured by FDM with a 2 cm × 2 cm top projected dimension.

Keywords: Osteochondral tissue engineering, PEDOT:PSS, Electroconductive scaffolds, Fused deposition modeling, Curved scaffolds, Mathematical modeling.

1. Introduction
Defects in the osteochondral (OC) tissue are a cause of joint malfunction and can lead to the development of degenerative diseases such as osteoarthritis (OA). An estimate by the World Health Organization has determined that 9.6% of men and 18.0% of women over the age of sixty suffer from symptomatic OA, and among them, 80% have limitations in mobility and 25% are unable to perform major daily activities. Due to the poor self-repair capabilities of articular cartilage (AC), OC defects tend to aggravate with time[1].

The OC tissue is a highly organized and complex structure located at the end of long bones, consisting of AC, calcified cartilage and subchondral bone[2,3]. The existence of a fine interplay between OC components makes them tightly interconnected under physiological conditions[3]. Figure 1 shows a schematic representation of OC tissue gradient features. With a distinct variation along its perpendicular direction, in terms of structure and composition of the extracellular matrix (ECM) as well as chondrocyte morphology, four distinct zones can be identified within the AC[4]. At the top, farthest from the bone, the superficial/tangential zone is the thinnest, making up 10-20 % of its height[5]. Here, chondrocytes synthesize more collagen and less proteoglycans relative to other zones and the water amount is also higher. The fibrils are tightly packed and parallel to the surface[6]. Immediately beneath is located the middle/transitional zone, making up around 50 % of AC height[7], and in which the collagen fibrils are thicker and randomly oriented. There is more proteoglycan and less collagen and water than in the previous zone[6]. Bellow, the deep/radial zone makes up around 35 % of the AC height[7]. The collagen fibrils have the largest diameter and are bunched up oriented perpendicular to the surface. It has the higher proteoglycan and the lower water contents[5]. The calcified cartilage layer is a thin layer bellow the deep zone, where the ECM contains a high concentration of calcium salts, and is located directly above the subchondral bone[8]. A thin wavy border, known as tidemark, marks the border between the deep zone and the calcified cartilage[9]. Collagen fibers run continuously between these two zones, strengthening this connection[7]. Chondrocytes in this zone express a hypertrophic phenotype and produce a network rich in type X collagen[10]. This layer, being permeable to small nutritional solutes of low molecular weight, plays an important role in maintaining the distinct microenvironments of AC and bone[5]. Subchondral bone and AC form what is designated as an OC unit.

Despite some recent progress, current treatment options for OC defects fail to fully recapitulate native tissue properties and structure, compromising long-term clinical results. The emergence of tissue engineering (TE) has opened new horizons for the establishment of new treatments[11–13]. TE strategies comprise three key components: cells, signaling factors, and biomaterial scaffolds[5,14].

The cells should ideally be easily expandable, non-immunogenic and express a protein pattern similar to the host tissue[11]. However, there are few cell types to choose from, and there are limitations in the available cell populations[15]. Cell sources used in OC TE usually fit into one of two groups, either progenitor cells (e.g., mesenchymal stem/stromal cells (MSCs)) or tissue specific cells (e.g., chondrocytes or osteoblasts)[12,16,17].

Signaling factors play a significant role in OC TE, regulating critical processes such as cell growth, differentiation and tissue homeostasis. These factors can be biochemical, physicochemical or physical in nature and modulate cell behavior by the activation of relevant pathways and expression of specific proteins[5,13,18].

In general, a scaffold should emulate structurally and functionally the native OC tissue. Not intended, by design, to be a permanent structure, they should be biodegradable and provide the appropriate microenvironment to promote cell differentiation and ECM production[5,19]. A wide variety of materials have been used to fabricate scaffolds in OC TE strategies, which are usually grouped in natural or synthetic polymers, inorganic materials, ECM-based materials, metals, and composites of the aforementioned ones.

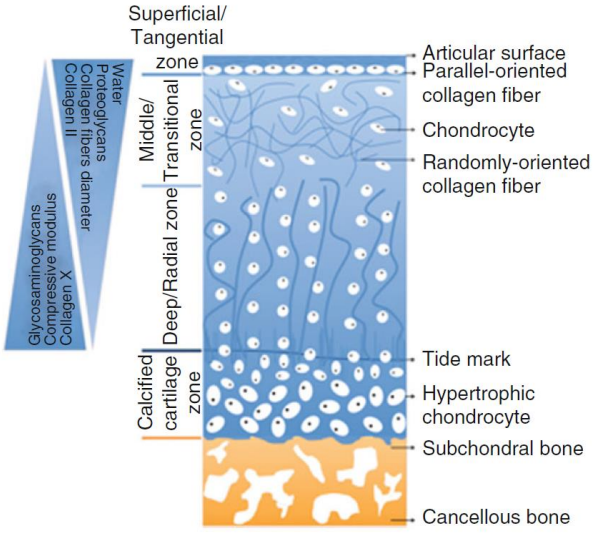

Figure 1 – Schematic representation of osteochondral tissue composition and organization (adapted from [16]).

Considering that tissues are responsive to electrical stimulation (ES), conducting polymers (CPs) became attractive to biomedical applications, such as bioactuators, biosensors, neural implants, drug delivery systems, and TE scaffolds[20,21]. Owing to its characteristics, poly(3,4-ethylenedioxythiophene) (PEDOT) has become one of the most used and studied CP in TE. It possesses a high conductivity and high stability in its oxidized state, and can be coupled with another polymer, poly(styrene sulfonate) (PSS), creating a water based stable colloidal suspension, which also has the effect of improving its conductivity[22]. Further strategies have been developed to enhance some of its properties, namely conductivity and adhesion. One method found to improve conductivity was the use of a co-solvent, with a proposed mechanism that involves the intercalation of the solvent molecules between the PEDOT and the PSS moieties, which leads to the stabilization of linear forms of the PEDOT chain. Maintaining the adhesion is a requirement for long term applications, and the poor mechanical stability of PEDOT:PSS is a major drawback. To address this limitation, the addition of cross-linkers such as (3-glycidyloxypropyl) trimethoxysilane (GOPS) or divinyl sulfone (DVS) is the most explored strategy[22].

Many features of TE scaffolds are related to scaffold geometry, which is closely related to the manufacturing technology[23]. Available 3D fabrication technologies can be divided into two main categories, conventional methods and additive manufacturing (AM), each producing scaffolds with different characteristics[24]. Although conventional techniques are still often used, they have known limitations for the fabrication of complex 3D constructs, which restrict their scope of applications, namely: rely on manual intervention and are poorly scalable and reproducible; offer limited ability to control shapes and geometries; use organic solvents and porogens[24–27]. More recently, AM has been applied to overcome the abovementioned limitations[24,25,27]. AM allows the process automation and high level of control over the fabricated constructs, guaranteeing its reproducibility and enabling scale-up and standardization. It also allows the flexibility of designing personalized constructs, important to meet patient individual needs, and offers the possibility of incorporating cells and bioactive materials[27–29].

The main objective of this thesis is the development of novel AM-based scaffold structures as well as new methods to tune their electrical conductivity. Novel electroconductive coatings for PCL scaffolds, based on PEDOT:PSS are proposed and characterized. Regarding the scaffold structure, two main strategies are outlined. In the first one, methods are proposed for the fast design and manufacture of 3D printed scaffolds, specifying the variation in pore geometry. In the second, the design and manufacture of two types of curved scaffolds is described. The first type concerns curved scaffolds mimicking the native curvature of OC tissue, enabling the creation of constructs for personalized therapies. The second type concerns scaffolds with a fully defined curvature and the computational determination of its mechanical properties.

2. Materials and Methods

2.1. Modeling software and manufacturing device

Models were created in Autodesk Fusion 360 student edition computer-aided design (CAD) software. Fused deposition modeling (FDM) 3D printing was done in a Prusa i3 MK3S 3D printer (Prusa Research, Praha, Czech Republic), with a 0.25 mm nozzle (Prusa Research). Materials were used in the format of 1.75 mm diameter filaments. Flexible filament from MakerBot (Poly(ϵ-caprolactone) (PCL), estimated density of 1.12 g/cm^3 [30]), and Poly(lactic acid) (PLA) from Velleman (1.24 g/cm^3) were used for 3D printing. The slicer software PrusaSlicer (Prusa Research) was used to create the G-code files that contain the machine-readable information to print each object.

2.2. Model fabrication profiles

3D printing profiles were created based on pre-tuned PrusaSlicer existing profiles. Concerning print settings, the “0.15 mm QUALITY” profile was the one adapted. Concerning the filament settings, for PLA, the default “Prusament PLA” profile was used, and for PCL a new profile was created, using the “Prusament PLA” profile as template, and with the following changed parameters: filament density to 1.12 g/cm^3; first layer nozzle temperature to 95°C; other layers nozzle temperature to 90°C; first layer bed temperature to 40°C; other layers bed temperature to 40°C; full fan speed at layer 1. Concerning the printer settings, the “Original Prusa i3 MK3S & MK3S+ 0.25 nozzle” profile was used, when printing with PLA. To print with PCL, a profile was created, based on the one used to print with PLA, only with a difference in the Start G-code, where

the instruction “M302 S75” was added to allow cold temperature extrusion. When printing with PCL, a further adjustment was implemented: printing speed was always reduced to 50% in the printer console, to improve printing quality.

2.3. PEDOT:PSS-coated PCL films manufacturing and characterization

PCL films manufacturing

Films with a parallelepipedal shape (20 mm × 10 mm × 1 mm) were designed and fabricated by FDM. In order to have films with a smoother surface to assess the coating characteristics, the following modifications were made to the default printing profile, for the first printed layer of the films: 0.15 mm extrusion width; 2 perimeters; 100 % infill/perimeter overlap; 1.2 extrusion multiplier.

PCL alkaline treatment

An alkaline treatment was employed to increase the number of hydroxyl and carboxyl hydrophilic groups on the surface of PCL. Films were fully immersed in a 1 M sodium hydroxide (NaOH, Sigma) aqueous solution for 24 h. After exposure, the films were rinsed three times with distilled water to ensure the finalization of the treatment and let to dry overnight at 37°C.

Coating and crosslinking protocol

Three strategies were used for the coating of PCL films and scaffolds with the objective of improving their electroconductivity. These strategies were applied to pristine PCL films and to alkaline treated films (PCL(NaOH)), according to the following protocols:

i) PEDOT:PSS dispersion (Clevios PH 1000, Heraeus Holding GmbH);

ii) PEDOT:PSS+GOPS dispersion, adding the dopants ethylene glycol (EG) (1:4 volume parts, Sigma-Aldrich), dodecylbenzenesulfonic acid (DBSA) (0.5 µL mL^{-1}, Sigma-Aldrich) and (3-glycidyloxypropyl)trimethoxysilane (GOPS) (10 µL mL^{-1}, Sigma- Aldrich);

iii) PEDOT:PSS+GOPS dispersion, adding the dopants ethylene glycol (EG) (1:4 volume parts, Sigma-Aldrich), dodecylbenzenesulfonic acid (DBSA) (0.5 µL mL^{-1}, Sigma-Aldrich) and divinyl sulfone (DVS) (30 µL mL^{-1}, Sigma-Aldrich).

Films were fully immersed in these dispersions for 24 h, at room temperature. Then, excess dispersion solution was absorbed from the surface of the films with paper towels and the samples were allowed to anneal for 24 h at 55°C.

Coating stability assay

To determine the coating stability, PEDOT:PSS-coated films were submerged in phosphate-buffered saline (PBS, Gibco) and placed in an incubator at 37°C and 5% CO_2. At the defined time points (0, 1, 7, 14, and 21 days) films were collected and washed three times with distilled water and let to dry overnight at 37°C.

Electroconductivity

The electroconductivity of the coated films was measured with the standard four-point probe method. For that purpose, four stripes of gold were deposited over the films by physical vapor deposition with an Edwards E306A thermal evaporator, across the entire films and with equal distance from each other. Measurements were done in triplicate. Applying a range of currents at the outer contacts, potential differences were measured between the two inner contacts. Using Ohm’s law, the resistance, *R,* is given by the slope between the potential and the current (*R=V/I*). At a constant temperature, the resistance of the sample, *R*, is proportional to its resistivity, *ρ*, and to the separation between the two inner contacts, *L*, and inversely proportional to the cross-section, *A* (product of the coating thickness, *t*, by its width, *w*), as described by equation (1).

$$R = \rho \times \left(\frac{L}{A}\right) \ [\mathrm{S}^{-1} \ or \ \Omega] \qquad (1)$$

Therefore, electroconductivity, *σ*, was obtained calculating the reciprocal of the determined resistivity, using equation (2).

$$\sigma = \frac{1}{\rho} \ [\mathrm{S\ cm}^{-1}] \qquad (2)$$

Coating thickness, *t*, was measured with a Bruker’s Dektak 3.21 Profilometer. With a scalpel, the coating superficial layer was scrapped off, until reaching the PCL film. The thickness was measured upon surface scanning perpendicularly to the cut.

Attenuated total reflectance-Fourier-transform infrared (ATR-FTIR) spectroscopy

ATR-FTIR analysis was performed using a Spectrum Two FT-IR Spectrometer (Perkin-Elmer, Waltham, MA, USA). Transmittance spectra were collected over the region from 400 to 4000 cm^{-1}, with a resolution of 1 cm^{-1}, at room temperature and using 8 scans.

Contact angle

Contact angle measurements were performed through the sessile drop method using a Krüss DSA25B goniometer. A drop of distilled water was deposited on the surface of the various films and its shape recorded every 0.5 s for 1 minute, to allow drop stabilization. Seven replica measurements were done for each condition and results were analyzed using the software Drop Shape Analysis 4 version 2.1.

2.4. Scaffold fabrication and characterization

Coated scaffolds manufacturing

PCL scaffolds, with the objective of being coated with the PEDOT:PSS dispersions, were designed in Fusion 360 and manufactured by FDM. The chosen dimensions for these scaffolds were 10.5 mm × 10.5 mm × 3 mm, with a 0-90° lay-down pattern. The selected size for the pore and for the scaffold fibers was 300 µm. Printing layer height was set to 150 µm, meaning that two layers were necessary to print each scaffold fiber. The default profiles created to print with PCL were used, with the following modifications: in the print settings, first layer height set to 0.15 mm, detect thin walls option checked, minimum of 2 loops for the skirt, a 2 layer height for the skirt, travel speed for non-print moves reduced to 45 mm/s, and extrusion width for the first layer set to 0.25 mm; in the printer settings, the retraction length was increased to 1.2 mm, the Z lift (when there is a retraction) increased to 0.3 mm, and

the extra length on restart (after a retraction) increased to 0.12 mm.

Curved scaffolds manufacturing

The curved scaffolds were printed with PLA, with the following modifications to the default profile: in the print settings, first layer height set to 0.15 mm, detect thin walls option checked, a 1 layer skirt height, travel speed for non-print moves reduced to 45 mm/s, and extrusion width for the first layer set to 0.25 mm; in the filament settings, nozzle temperature for the first an all other layers was set to 210°C, and the bed temperature for the first and all other layers was set to 65°C; in the printer settings, the retraction length was increased to 1.2 mm, and the Z lift (when there is a retraction) was increased to 0.3 mm.

Compressive mechanical testing

The scaffolds were evaluated under uniaxial compressive mechanical testing using a TA.XT*plus*C Texture Analyser (Stable Micro Systems, Godalming, Surrey, United Kingdom) equipped with a 50 kg load cell. A displacement rate of 1 mm/min was used and six different scaffold specimens (n=6) were tested for each condition. Exponent Connect software (Stable Micro Systems) was used to collect and process the experimental data. The compressive moduli were calculated from the slope of initial linear regions in the stress-strain curves and, when possible, the maximum stresses were determined from the maximum of the stress-strain curve.

Micro-computed tomography analysis

Internal microstructure images of PCL scaffolds were obtained using micro-computed tomography (micro-CT) with a SkyScan 1174v2, Bruker version 1.1 (Bruker, Billerica, MA, USA). Image reconstruction was performed using NRecon Program Version 1.6.8.0 (Bruker), CTVox and CTVol softwares version 2.3.2.0 (Bruker) were used to obtain realistic 3D visualizations of the scanned scaffold samples, and CTAn version 1.20.0 software (Bruker) was used for image analysis. The acquisition parameters depended on the sample being analyzed. With the scaffolds for electroconductivity assays, the following parameters were used: source voltage of 50 kV; source current of 800 mA; image pixel size of 14 µm; exposure time of 6000 ms; rotation step of 0.5°; frame averaging on (2); no filter. For the curved scaffolds, the following parameters were used: source voltage of 50 kV; source current of 800 mA; image pixel size of 30.11 µm; exposure time of 9000 ms; rotation step of 0.5°; frame averaging on (3); no filter.

Computational simulation of compressive mechanical behavior of curved scaffolds

Finite element analysis (FEA) was performed using the Solid Mechanics (solid) module from COMSOL Multiphysics 5.5 software (Sweden). A stationary study was considered, with the aim of determining the stresses when scaffolds are subjected to compressive load. Sections of the scaffolds in STEP format were imported into COMSOL, where a physics-controlled mesh with extra-fine element size was used to generate the elements of the model. The assigned scaffold material was PLA, from the software materials library. For the solid mechanics studies, the faces of the scaffold corresponding to the AC side were subjected to a boundary load of 1 MPa, and the faces of the scaffold corresponding to the subchondral bone side were constrained to a fixed position. Results were calculated for the von Mises Stress (solid.mises plot) and for displacement (solid.disp plot).

2.5. Statistical analysis

The results, when applicable, are presented as mean values ± standard deviations (SD). The statistical analysis was performed using GraphPad Prism 9.2 (GraphPad Software, San Diego, CA, USA). To assess statistically significant differences between independent samples, ANOVA tests were performed followed by Tukey's multiple comparison test. Statistically different values were considered for p-value < 0.05 (95% significance level; * denotes p<0.05, ** denotes p<0.01, *** denotes p<0.001, **** denotes p<0.0001).

3. Results and Discussion

A preliminary assay was performed to measure the electroconductivity with the four-point probe method on the surface of films that were coated following the six strategies described previously, without submerging them in PBS (Day 0, data not shown). Both cross-linking strategies improved noticeably electroconductivity in relation to the coating only with PEDOT:PSS. Another assay showed that coatings only with PEDOT:PSS, without any cross-linker, were much more brittle (data not shown). For these reasons, it was decided to run the 21 days stability assay only with films coated using the protocols including the cross-linkers. Figure 2a shows the results of the electroconductivity measurements on the coated films. Electroconductivity values do not show any significant variation throughout the 21 days of the experiment, confirmed by the 2-way ANOVA test: at a significance level of 5%, the variation between the five time points, the variation between the four coating strategies, and the interaction variation were all non-significant. There was no substantial decrease in conductivity in relation to day 0, giving an indication that the coatings are stable and not delaminating. The mean values are in the range 3.0-26 S/cm, close to values already used in cell ES studies[31]. Standard deviation error bars are considerably large, suggesting a high variability in the measurements. The reason may be related with the need of scraping the PEDOT:PSS coatings from the surface of the films, and due to the softness of PCL in relation to the scalpel used some PCL may have been removed together with the coating. Thus, from Figure 2a, it was not possible to identify a coating strategy having a better performance in relation to the others.

Figure 2b depicts the obtained ATR-FTIR spectra. Concerning the two coating dispersions (PEDOT:PSS(GOPS) and PEDOT:PSS(DVS)), the spectra are dominated by the ethylene glycol that is also present in the coating formulations and is identified by its characteristic peaks [32,33], and the weak PEDOT:PSS peaks between 400 cm^{-1} and 1600 cm^{-1} are not discernible[34]. The reduced volumes of GOPS, DVS, and DBSA present in the coating dispersions also prevent the detection of the corresponding peaks.

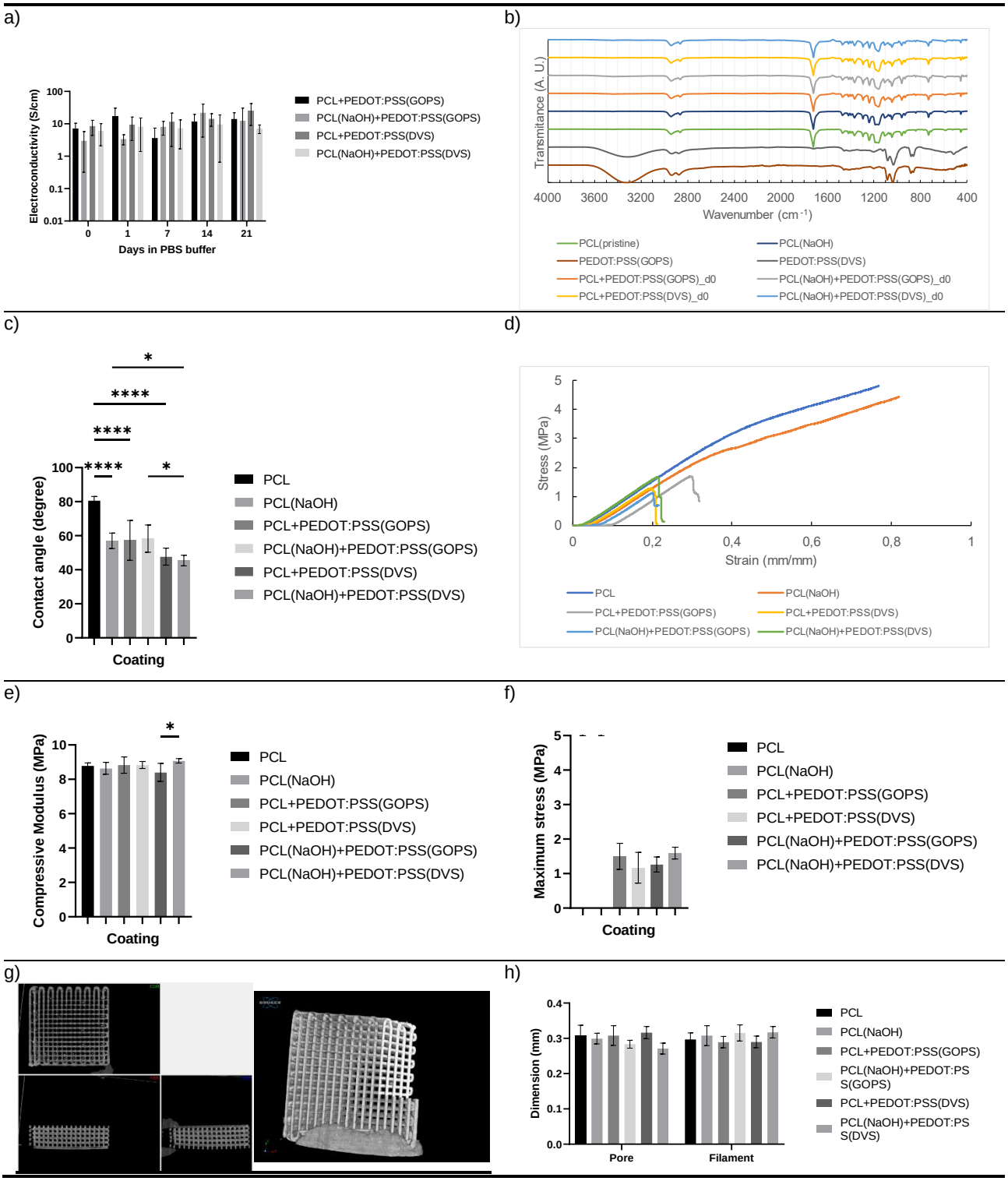

Figure 2 – PEDOT:PSS-coated films and scaffolds characterization: a) Calculated conductivity with the four-point probe method for the coating stability assay. Conductivity was measured on coated PCL films submerged in PBS at 37°C and 5% CO2. Films were collected to be analyzed on days 0, 1, 7, 14, and 21 of the stability assay. Results are expressed as mean ± SD (n=3). (Electroconductivity log scale); b) ATR-FTIR spectra of samples of uncoated PCL films, samples of coating dispersions, and samples of PEDOT:PSS-coated PCL films collected at day 0 of the stability assay; c) Contact angle on the surface of uncoated and coated PCL films determined by the sessile drop method. Coated films were collected to be analyzed on day 0 of the stability assay. Results are expressed as mean ± SD (n=7); d) Representative compressive stress-strain curves of uncoated and PEDOT:PSS-coated PCL scaffolds; e) Compressive Young's modulus of uncoated and PEDOT:PSS-coated PCL scaffolds. Results are expressed as mean ± SD (n=5); f) Estimated maximum stresses of uncoated and PEDOT:PSS-coated PCL scaffolds. Results are expressed as mean ± SD (n=5); g) Micro-CT imaging reconstructions. Left: representative pictures of coronal, transverse, and sagittal cuts of a PCL scaffold (PCL+PEDOT:PSS(GOPS) scaffold in the picture). Right: representative 3D reconstruction, with a cut section, of a PCL scaffold (PCL(NaOH)+PEDOT:PSS(DVS) scaffold in the picture); h) Pore and fiber dimensions of uncoated and PEDOT_PSS-coated PCL scaffolds, estimated from measurements in transverse cuts obtained from micro-CT imaging. Results are expressed as mean ± SD (n=3).

Concerning the uncoated and PEDOT:PSS-coated PCL films, due to the very thin coating layer that was deposited, the spectra are dominated by the PCL characteristic peaks[35]. With these substances showing

such a dominance in the spectra, it is not possible to analyze the chemical reactions occurring during annealing between PEDOT:PSS, the cross-linkers, and other substances. The effect of alkaline treatment on the spectra is also not noticeable, most likely because it is only superficial.

Hydrophilicity of the PEDOT:PSS-coated films and of the uncoated films was determined measuring the contact angle (Figure 2c). In the tested samples, PCL is the least hydrophilic and all other samples are more hydrophilic. Significant differences were found in all pairwise comparisons with pristine PCL. Using DVS as a crosslinker seems to have a greater effect increasing hydrophilicity, but only the comparison between PCL(NaOH)+PEDOT:PSS(GOPS) and PCL(NaOH)+PEDOT:PSS(DVS) was statistically significant. From previous works[36], it was expected that pristine PCL would have a contact angle above 90°, however it was not confirmed. Possible explanations are that some hydrolytic degradation might already have occurred on the filament material due to being stored exposed to the laboratory environment, or that some other components may be present in the purchased PCL filament. Concerning the alkaline treatment, the change to the film surface was confirmed, verified by the decrease in the contact angle, in relation to the untreated films (PCL vs. PCL(NaOH)). The alkaline treatment also did not seem to interfere with the coating procedure. The two coatings with PEDOT:PSS(GOPS) did not show a significant difference between them, and the same happened with the two coatings with PEDOT:PSS(DVS).

Figure 2d shows representative stress-strain curves of analyzed coated scaffolds. One substantial difference was seen between the PEDOT:PSS-coated and uncoated PCL scaffolds. All coated scaffolds shattered during the compression test, while the uncoated scaffolds, although plastically deformed, maintained structural integrity. A plausible explanation may be in the acidic PEDOT:PSS dispersion used in the coating procedure causing an acid catalyzed degradation of PCL, which has been described[37]. Also, some structural modifications to the PCL during annealing should not be ruled out. This process was carried out at 55°C for 24 hours, close to the estimated PCL melting temperature (~60°C), which may have led to polymer chain rearrangements. Considering the compression moduli, calculated from the initial linear regions of the stress-strain curves, all were very similar, only significantly different when comparing PCL(NaOH)+PEDOT:PSS(GOPS) with PCL(NaOH)+PEDOT:PSS(DVS) (Figure 2e). Neither the alkaline treatment nor the possible effect of the acidic PEDOT:PSS coating dispersion evidenced an effect in the moduli. The maximum stresses for the coated and uncoated scaffolds are represented in Figure 2f. Uncoated scaffolds deformed plastically but did not break, while maximum stress was achieved for the coated scaffolds. However, there is no significant difference between the determined maximum stress values.

Representative images of the scaffold micro-CT reconstructions are shown in Figure 2g. In order to determine the accuracy of the printing process, for each scaffold, the transverse cut was used to measure the dimension of 3 consecutive pores and fibers. Figure 2h shows an agreement between the designed pore and scaffold fiber dimensions, both designed with 0.3 mm, and the calculated values of those two features. Some variations around the 0.3 mm can be accounted by some experimental imprecision in selecting the correct plane for the transverse cut. At a significance level of 5%, no differences were determined between the estimated dimensions of the scaffolds.

From all gathered evidence in the film and scaffold characterizations, there was no clear distinction between the coating strategies, supporting one strategy over the others. Further characterization could prove beneficial, namely scanning electron microscopy (SEM) analysis of both films and scaffolds to verify the effect of the alkaline treatments on PCL and possibly verify coating thickness, to differentiate between coating strategies.

In recent years, AM has introduced new possibilities to the field of TE, owing to the higher control in the design and manufacture of scaffold structures[38,39]. Using medical imaging techniques like magnetic resonance imaging (MRI) and computer tomography (CT) to obtain 3D models of tissues and processing them via CAD software is expected to allow the creation of constructs reproducing the correct shape of tissues and also patient specific to fit individual defects[40–42]. With that in mind, a model was designed in a way that the curvature could be quantifiable. The chosen hypothesis was to think of a scaffold which curvature would follow a cutout of the surface of a sphere (Figure 3a). Then, the radius of that sphere would give a measure of the curvature of the scaffold. Having a method to design scaffolds with any arbitrary curvature, the question then became to assess the possibility of manufacturing them by FDM. Increasing the curvature, the print would be closer to the situation where the filament being deposited would not be supported by the layer underneath, in which situation the print would fail (Figure 3b). The design objective then became to determine the curvature at which, in the extremities of the scaffold, there would be the bare minimum contact between adjacent layers. Mathematically, this translated into having a tangential alignment between the walls of deposited filaments in consecutive layers (Figure 3c). Figure 3d-e shows the systematization of the problem being solved. The line representing the axis of symmetry (grey dashed line) is the reference for the variables L (half the height of the scaffold), α (angle to the position of the second fiber of the scaffold), and β (angle to the position of the first fiber of the scaffold). R is the curvature of a circle when a cross-section of the scaffold is done. Fiber dimensions are also indicated: 300 µm fiber width and 150 µm printing layer height (two layers for each fiber). *Distance* represents the horizontal distance between the positions where the two fibers are deposited. The variables can be related by Equations (3). Since there are three equations and five variables, values need to be assigned to two variables to find a solution. Values had already been assigned to L (10.05 mm) and to *distance* (0.3 mm), so it was possible to calculate the more extreme value for R. Two strategies were used to

calculate *R*. One graphical, using Fusion 360, and one analytical, using Mathematica 12.3. Both strategies returned the same solutions: R = 13.7902 mm; α = 44.1186°; β = 45.8814°.

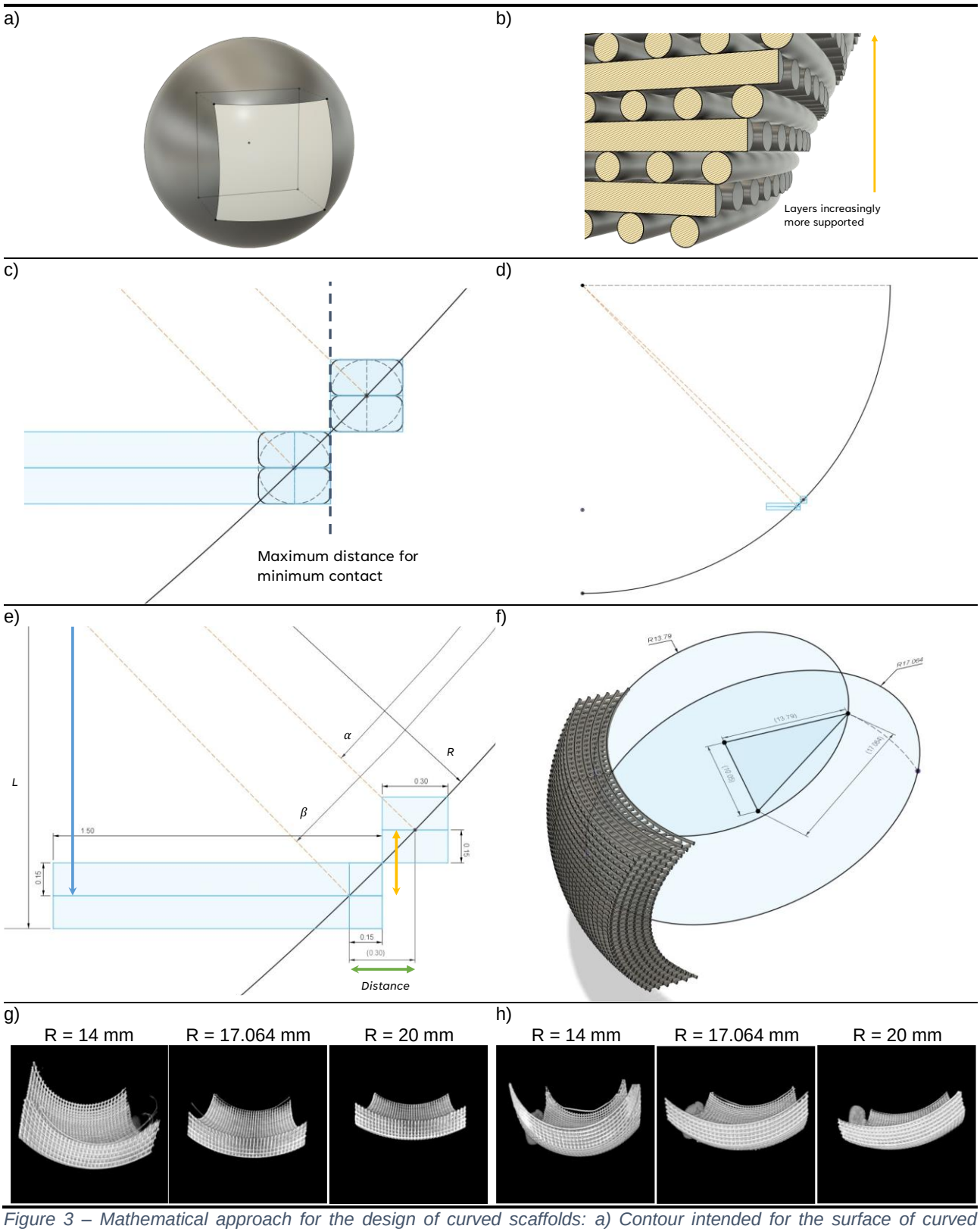

Figure 3 – Mathematical approach for the design of curved scaffolds: a) Contour intended for the surface of curved scaffolds, represented by the bright area. The curvature is defined by the sphere radius. Projected square shape has a 20.1 mm side; b) Cross-section, through the middle of the scaffold, observing decreased layer support closer to the base of the print; c) Minimum contact between adjacent layers when maximum curvature is reached; d) Wide view and e) Close-up of the base of the scaffold where the extreme minimum contact situation will occur. The light blue structures represent the first fibers being printed, on top of the printer bed. Since the scaffold is symmetric, only the bottom half is represented. R – radius of circular cross-section; L – vertical distance to the axis of symmetry of the scaffold (grey dashed line); α, β – angles measured from the axis of symmetry of the scaffold (grey dashed line); f) Calculation of the sphere radius (17.064 mm) defining scaffold surface curvature from the radius calculated to provide minimum support between scaffold fibers (13.7902 mm); g) Micro-CT imaging reconstructions of scaffolds designed with concentric radius strategy; h) Micro-CT imaging reconstructions of scaffolds designed with constant radius strategy.

$$\begin{cases} distance = R(\cos\alpha - \cos\beta) \\ R(\sin\beta - \sin\alpha) = 2 \times 0.15 \\ Rsin\,\beta = L - 0.15 \end{cases} \quad (3)$$

The previous deduction for *R* applies to the radius of circles parallel to the ones in Figure 3f, the same as the orientation of the cut in Figure 3b-c. It can be seen that towards the edges the radius is smaller, compared to the radius through the middle of the scaffold. The extreme calculated case corresponds to the circles on the edge. To find the radius of the circle through the center of the scaffold, which is also the radius of the sphere defining the surface curvature of the scaffold, the Pythagorean theorem can be used (Figure 3f). The calculated sphere radius is then 17.064 mm.

Two strategies were elected to give the scaffold its thickness: i) designated constant radius, all curved surfaces used to trace the path of scaffold fibers have the same radius; and ii) designated concentric radius, a series of concentric curves are used to trace the path of scaffold fibers. These strategies have consequences on their overall shape and pore dimensions. With the concentric strategy, the thickness of the scaffold is greater at the edges than at the center. On the contrary, with the constant radius strategy, the thickness is smaller at the edges than at the center. Due to that variation, the projected pore area on the top layer increases towards the edges with the concentric strategy and decreases towards the edges with the constant radius strategy. These differences can be appreciated comparing the micro-CT reconstructions in Figure 3g and Figure 3h. From these reconstructions, it can also be seen that some fibers at the edge of the scaffolds are detached, and more noticeably in the scaffolds with a smaller radius. In the scaffolds with 14 mm radius, edge fibers are seen completely detached and distorted while in the scaffolds with 17.064 mm the extremities of fibers are seen detached, and in the scaffolds with 20 mm, although the fibers were printed respecting the curvature of the design, the contact points of the edge fibers do not seem the most robust.

For the simulation of the compressive mechanical behavior, one scaffold was selected to demonstrate the calculations results (20 mm radius and concentric curved surfaces). Due to the complexity of the curved scaffold model, generating a file too big for COMSOL to handle, the simulation could not be done using the entire model. The alternative was to select relevant regions of interest in the scaffold, run the simulation on those regions, and then extrapolate the results for the entire scaffold. Figure 4 shows those selected regions. Figure 5a-c show respectively the von Mises stress for the center, the corner, and the slice of the scaffold, that allows to determine if the material will yield under the applied load. It can be seen that the greater stresses are predicted for the fiber connections in the front of the scaffold, where the load is applied, and the value is significantly higher in relation to the stresses in every other region of the scaffold. Besides these extremes, it is also in the other fiber connections that the stress is higher, but within the same magnitude values as the maximum in the rest of the scaffold. It can also be seen that the fibers that run from the front to the back of the scaffold show an evenly distributed stress except in the front, where the load is applied. Due to the fact that only sections of the scaffold were modeled, some observations need a more careful analysis. In Figure 5a, the two fibers at the top and bottom of the section, show very high stresses because the fibers that exist above and below them in the complete scaffold were not considered in the model. The maximum stress values calculated in this simulation are then overestimated because it does not account for more fibers. A comparable situation is seen in Figure 5b. Since only a small section from the corner was modeled, the simulation predicts that it bends upwards with the applied load. However, from Figure 5c it can be anticipated that this bending would not be seen in a complete scaffold because the fibers below would prevent it from happening. Figure 5c also confirms the intuition that the fibers at the edge of the scaffold will be the ones more susceptible of yielding. The farther the fibers are from the wireframe structure and larger they are, the greater the deformation.

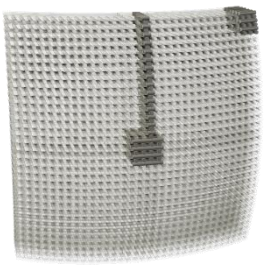

Figure 4 – Regions of interest for finite element analysis of the mechanical behavior in an illustrative curved scaffold (20 mm concentric).

4. Conclusions and future work

ES is known to guide the development and regeneration of many tissues. To allow the study of its effect in OC TE constructs, six different coating conditions were evaluated to functionalize non-electrically conductive 3D-printed PCL scaffolds. The coating strategies combining the cross-linkers GOPS or DVS with the PEDOT:PSS dispersion proved to be superior, maintaining structural integrity and providing adequate, stable, and long-lasting electric conductivity. The surface modification of PCL, attained with an alkaline treatment, increasing hydroxyl and carboxyl groups at its surface, did not seem to influence the performance of the coating strategies, with determined properties very similar to those of coatings done to pristine PCL. Comparing the two cross-linker coating strategies, with GOPS or DVS, no particularly significant differences were identified between them. On the contrary, the impact of the coating and annealing procedure on the mechanical properties of all PEDOT:PSS-coated scaffolds was significant. Future work will include *in vitro* cell culture assays to study the coatings biocompatibility and the scaffolds biological performance. ES protocols could then be explored to study their influence in the cell differentiation towards the production of increasingly native-like OC TE tissue constructs.

Considering the mathematically defined curved scaffolds, the micro-CT reconstructions point to the confirmation of the premises behind their modeling. With increased curvature, the contact points between fibers start become increasingly weaker and more

easily detachable. These differences in adhesion, together with the novelty of this geometry, advise for their mechanical characterization in the future, which would be particularly interesting to compare with the mechanical properties of more conventional orthogonal scaffolds. Further developments could also be considered for these curved scaffolds, namely, the use of more parameters to control the scaffold curvature in order to allow the fabrication of more organic biomimetic shapes.

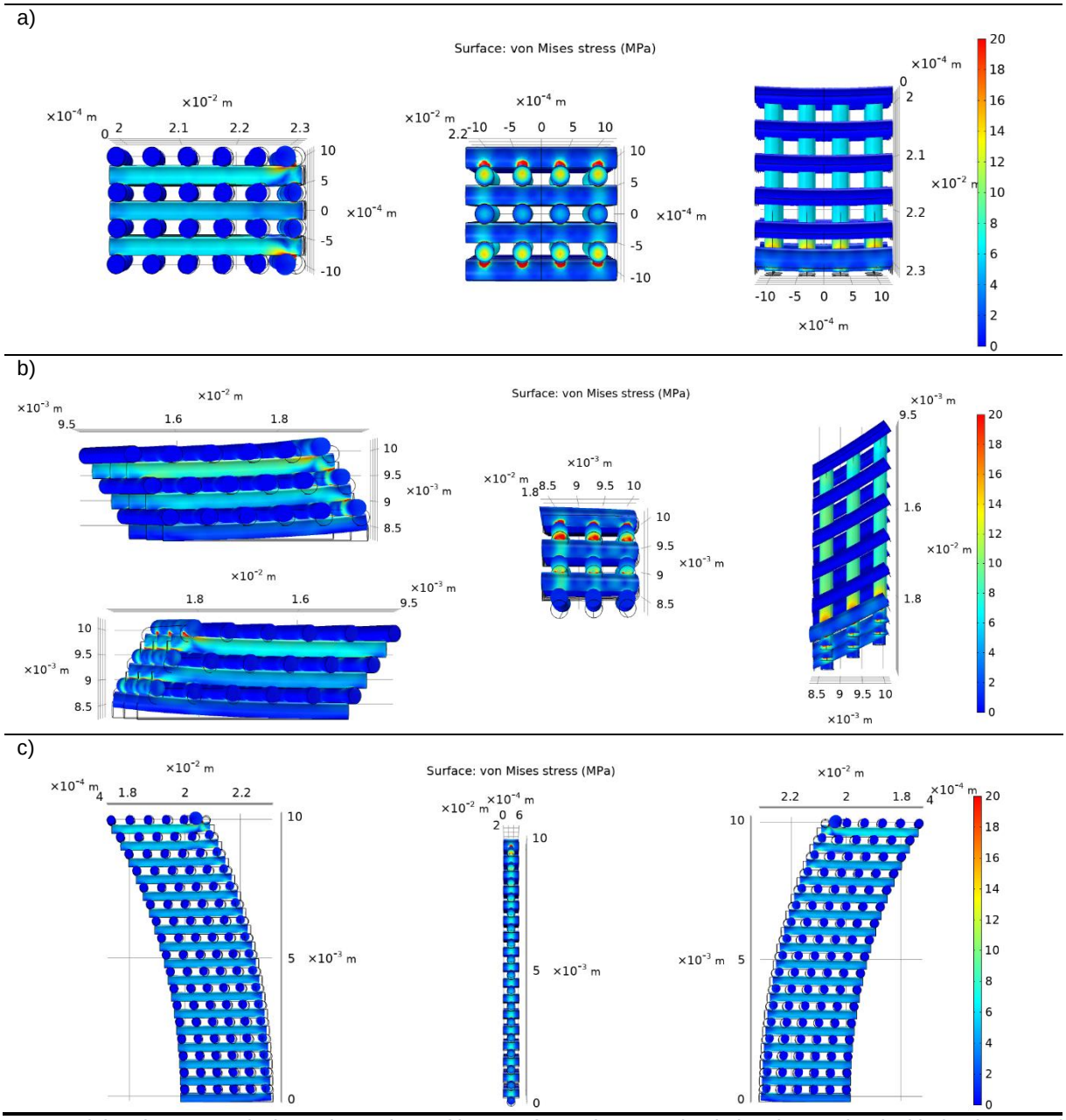

Figure 5 – Finite element analysis on the regions of interest from Figure 4, simulating the mechanical behavior to regions of interest of a PLA scaffold when 1 MPa load is applied on the front surface and the back is considered fixed: a) Side, front, and top views of the von Mises stress; b) Both sides, front, and top views of the von Mises stress; c) Side, front and opposite side views of the von Mises stress. (Scale bars truncated bellow the maximum to provide a better sense of the simulated behavior).

The experimental mechanical characterization of the curved scaffold will also be relevant to validate the mathematical simulation presented in this thesis. Having an accurate computational representation of the scaffold physics, in the form of a digital twin, will also provide major advantages in time and resources when investigating new OC TE scaffold designs.

Acknowledgements

I would like to thank my supervisors, Professor Frederico Ferreira and Doctor João Carlos Silva for their guidance and to the Centre for Rapid and Sustainable Product Development (CDRSP) of the Polytechnic Institute of Leiria for their assistance to this work. I would also like to acknowledge the funding received from the FCT through the project OptiBioScaffold (PTDC/EME-SIS/4446/2020).

References

1. Zhang, B., Huang, J. & Narayan, R. J. Gradient scaffolds for osteochondral tissue engineering and regeneration. *J. Mater. Chem. B* **8**, 8149–8170 (2020).
2. Alexander, P. G., Gottardi, R., Lin, H., Lozito, T. P. & Tuan, R. S. Three-dimensional osteogenic and chondrogenic systems to model osteochondral physiology and degenerative joint diseases. *Exp. Biol.*

Med. **239**, 1080–1095 (2014).
3. Di Luca, A., Van Blitterswijk, C. & Moroni, L. The osteochondral interface as a gradient tissue: From development to the fabrication of gradient scaffolds for regenerative medicine. *Birth Defects Res. Part C - Embryo Today Rev.* **105**, 34–52 (2015).
4. Deng, C., Chang, J. & Wu, C. Bioactive scaffolds for osteochondral regeneration. *J. Orthop. Transl.* **17**, 15–25 (2019).
5. Wei, W. & Dai, H. Articular cartilage and osteochondral tissue engineering techniques: Recent advances and challenges. *Bioact. Mater.* **6**, 4830–4855 (2021).
6. Temenoff, J. S. & Mikos, A. G. Review: tissue engineering for regeneration of articular cartilage. *Biomaterials* **21**, 431–440 (2000).
7. Baumann, C. A., Hinckel, B. B., Bozynski, C. C. & Farr, J. Articular Cartilage: Structure and Restoration. in *Joint Preservation of the Knee* 3–24 (Springer International Publishing, 2019). doi:10.1007/978-3-030-01491-9_1.
8. Cheng, H., Luk, K. D. K., Cheung, K. M. C. & Chan, B. P. In vitro generation of an osteochondral interface from mesenchymal stem cell–collagen microspheres. *Biomaterials* **32**, 1526–1535 (2011).
9. Bhosale, A. M. & Richardson, J. B. Articular cartilage: Structure, injuries and review of management. *Br. Med. Bull.* **87**, 77–95 (2008).
10. Karsdal, M. A. Introduction. in *Biochemistry of Collagens, Laminins and Elastin* xix–xxxiv (Elsevier, 2016). doi:10.1016/B978-0-12-809847-9.02001-8.
11. Salgado, A. J., Coutinho, O. P. & Reis, R. L. Bone tissue engineering: State of the art and future trends. *Macromol. Biosci.* **4**, 743–765 (2004).
12. Nukavarapu, S. P. & Dorcemus, D. L. Osteochondral tissue engineering: Current strategies and challenges. *Biotechnol. Adv.* **31**, 706–721 (2013).
13. Vinatier, C., Mrugala, D., Jorgensen, C., Guicheux, J. & Noël, D. Cartilage engineering: a crucial combination of cells, biomaterials and biofactors. *Trends Biotechnol.* **27**, 307–314 (2009).
14. Makris, E. A., Gomoll, A. H., Malizos, K. N., Hu, J. C. & Athanasiou, K. A. Repair and tissue engineering techniques for articular cartilage. *Nat. Rev. Rheumatol.* **11**, 21–34 (2015).
15. Ondrésik, M., Oliveira, J. M. & Reis, R. L. Advances for Treatment of Knee OC Defects. in *Osteochondral Tissue Engineering: Challenges, Current Strategies, and Technological Advances* (eds. Oliveira, J. M., Pina, S., Reis, R. L. & San Roman, J.) 3–24 (Springer International Publishing, 2018). doi:10.1007/978-3-319-76735-2_1.
16. Correia, C. R., Reis, R. L. & Mano, J. F. Multiphasic, Multistructured and Hierarchical Strategies for Cartilage Regeneration. in *Engineering Mineralized and Load Bearing Tissues* (eds. Bertassoni, L. E. & Coelho, P. G.) 143–160 (Springer International Publishing, 2015). doi:10.1007/978-3-319-22345-2_9.
17. Lopa, S. & Madry, H. Bioinspired Scaffolds for Osteochondral Regeneration. *Tissue Eng. Part A* **20**, 2052–2076 (2014).
18. Yousefi, A. M., Hoque, M. E., Prasad, R. G. S. V. & Uth, N. Current strategies in multiphasic scaffold design for osteochondral tissue engineering: A review. *J. Biomed. Mater. Res. - Part A* **103**, 2460–2481 (2015).
19. Turnbull, G. *et al.* 3D bioactive composite scaffolds for bone tissue engineering. *Bioact. Mater.* **3**, 278–314 (2018).
20. Guimard, N. K., Gomez, N. & Schmidt, C. E. Conducting polymers in biomedical engineering. *Prog. Polym. Sci.* **32**, 876–921 (2007).
21. Guo, B. & Ma, P. X. Conducting Polymers for Tissue Engineering. *Biomacromolecules* **19**, 1764–1782 (2018).
22. Piro, B. *et al.* Fabrication and use of organic electrochemical transistors for sensing of metabolites in aqueous media. *Appl. Sci.* **8**, (2018).
23. Fu, L. *et al.* Advances and prospects in biomimetic multilayered scaffolds for articular cartilage regeneration. *Regen. Biomater.* **7**, 527–542 (2020).
24. Roseti, L. *et al.* Scaffolds for Bone Tissue Engineering: State of the art and new perspectives. *Mater. Sci. Eng. C* **78**, 1246–1262 (2017).
25. Koons, G. L., Diba, M. & Mikos, A. G. Materials design for bone-tissue engineering. *Nat. Rev. Mater.* **5**, 584–603 (2020).
26. Leong, K. F., Cheah, C. M. & Chua, C. K. Solid freeform fabrication of three-dimensional scaffolds for engineering replacement tissues and organs. *Biomaterials* **24**, 2363–2378 (2003).
27. Gillispie, G. J. *et al.* Three-Dimensional Tissue and Organ Printing in Regenerative Medicine. in *Principles of Regenerative Medicine* 831–852 (Elsevier, 2019). doi:10.1016/B978-0-12-809880-6.00047-3.
28. Melchels, F. P. W. *et al.* Additive manufacturing of tissues and organs. *Prog. Polym. Sci.* **37**, 1079–1104 (2012).
29. Jeong, C. G. & Atala, A. 3D Printing and Biofabrication for Load Bearing Tissue Engineering. in *Engineering Mineralized and Load Bearing Tissues* (eds. Bertassoni, L. E. & Coelho, P. G.) 3–14 (Springer International Publishing, 2015). doi:10.1007/978-3-319-22345-2_1.
30. Fiedler, T. *et al.* On the mechanical properties of PLC-bioactive glass scaffolds fabricated via BioExtrusion. *Mater. Sci. Eng. C* **57**, 288–293 (2015).
31. Sordini, L. *et al.* Effect of Electrical Stimulation Conditions on Neural Stem Cells Differentiation on Cross-Linked PEDOT:PSS Films. *Front. Bioeng. Biotechnol.* **9**, (2021).
32. Çabuk, H., Yılmaz, Y. & Yıldız, E. Vortex-Assisted Deep Eutectic Solvent-Based Liquid-Liquid Microextraction for the Analysis of Alkyl Gallates in Vegetable Oils. *Acta Chim. Slov.* **66**, 385–394 (2019).
33. Haoue, S., Derdar, H., Belbachir, M. & Harrane, A. Polymerization of Ethylene Glycol Dimethacrylate (EGDM), Using An Algerian Clay as Eco-catalyst (Maghnite-H+ and Maghnite-Na+). *Bull. Chem. React. Eng. Catal.* **15**, 221–230 (2020).
34. Zhao, Q., Jamal, R., Zhang, L., Wang, M. & Abdiryim, T. The structure and properties of PEDOT synthesized by template-free solution method. *Nanoscale Res. Lett.* **9**, 557 (2014).
35. Phillipson, K., Hay, J. N. & Jenkins, M. J. Thermal analysis FTIR spectroscopy of poly(ε-caprolactone). *Thermochim. Acta* **595**, 74–82 (2014).
36. Moura, C. S. *et al.* Chondrogenic differentiation of mesenchymal stem/stromal cells on 3D porous poly (ε-caprolactone) scaffolds: Effects of material alkaline treatment and chondroitin sulfate supplementation. *J. Biosci. Bioeng.* **129**, 756–764 (2020).
37. Lam, C. X. F., Savalani, M. M., Teoh, S.-H. & Hutmacher, D. W. Dynamics of in vitro polymer degradation of polycaprolactone-based scaffolds: accelerated versus simulated physiological conditions. *Biomed. Mater.* **3**, 034108 (2008).
38. Bahraminasab, M. Challenges on optimization of 3D-printed bone scaffolds. *Biomed. Eng. Online* **19**, 1–33 (2020).
39. Mota, C., Camarero-Espinosa, S., Baker, M. B., Wieringa, P. & Moroni, L. Bioprinting: From Tissue and Organ Development to in Vitro Models. *Chem. Rev.* **120**, 10547–10607 (2020).
40. Kang, H.-W. *et al.* A 3D bioprinting system to produce human-scale tissue constructs with structural integrity. *Nat. Biotechnol.* **34**, 312–319 (2016).
41. Melchels, F. *et al.* CAD/CAM-assisted breast reconstruction. *Biofabrication* **3**, 034114 (2011).
42. Daly, A. C. *et al.* 3D Bioprinting for Cartilage and Osteochondral Tissue Engineering. *Adv. Healthc. Mater.* **6**, 1–20 (2017).